Integration of an Inorganic Semiconductor with a Metal–Organic Framework: A Platform for Enhanced Gaseous Photocatalytic Reactions

Rui Li, Jiahua Hu, Mingsen Deng, Helin Wang, Xijun Wang, Yingli Hu, Hai-Long Jiang, Jun Jiang, Qun Zhang,* Yi Xie, and Yujie Xiong**

Photocatalysis is a highly important route to solar-to-chemical energy conversion by mimicking the natural photosynthetic process. In photocatalysis, semiconductor materials are excited by light absorption to generate electron–hole pairs which are then separated and transferred to different sites for redox reactions.[1] Thus the quantum efficiency of materials in this process essentially relies on two key steps: charge separation, and molecular adsorption and activation. The latter step is particularly crucial to gaseous reactions in practical applications, as effective charge transfer from photocatalysts to gas molecules relies on their intimate and stable binding. For instance, the reaction between CO_2 and H_2O is a promising approach to recycling carbon sources into fuels;[2–4] however, it remains challenging to efficiently capture the CO_2 molecules by using photocatalytic materials. In the past, metal–organic frameworks (MOFs) were identified as a class of porous materials for gas capture and storage, owing to their capability to offer adsorptive sites for gas uptake.[5–9] In addition, MOF materials have demonstrated wide applications in molecular recognition, gas separation, catalysis, and drug delivery.[10–16] Nevertheless, the performance of MOFs in photocatalysis is not comparable to that of inorganic semiconductors; it is mainly limited by MOFs' low efficiency in exciton generation and charge separation. To boost the photocatalytic efficiency for gaseous reactions, an ideal solution would be to functionally integrate the gas adsorption into the MOF with exciton generation by an inorganic semiconductor. The key to this integration is whether the photoexcited electrons can be effectively transferred from the semiconductor to the MOF.

Herein, we demonstrate by using ultrafast spectroscopy that charge transfer can occur between photoexcited inorganic semiconductors and MOFs. This charge transfer substantially suppresses electron–hole recombination in the semiconductor, as well as supplies long-lifetime electrons for the reduction of gas molecules adsorbed on the MOF. For proof of concept, we develop a method for synthesizing $Cu_3(BTC)_2$@TiO_2 core-shell structures and examine their photocatalytic performance in gaseous reactions by using CO_2 conversion as a model system. TiO_2 is known as an inorganic semiconductor with photocatalytic activity for conversion of CO_2 into CH_4 (with the aid of H_2O), while $Cu_3(BTC)_2$ (BTC = benzene-1,3,5-tricarboxylate), namely HKUST-1,[17] has proven an excellent material for CO_2 storage.[18–20] The designed hybrid materials possess a unique structure (as schematically illustrated in **Figure 1**a): i) the semiconductor TiO_2 is formed as shells so it is easily photoexcited to generate excitons; ii) the shells are macroporous to facilitate the capture of gas molecules in the cores and to provide sufficient surface area for photocatalysis. The synthesis of hybrid structures between MOFs and inorganic materials was explored by several research groups.[21–23] For instance, Pd@ZIF-8 (zeolitic imidazolate framework 8) core-shell structures were synthesized for catalytic hydrogenation by using Cu_2O as an intermediate layer;[21] ZnO@ZIF-8 core-shell nanorods were prepared for photo-electrochemical sensing by converting ZnO surface into ZIF-8.[22] However, these hybrid structures cannot meet the criteria for photocatalytic CO_2 conversion mentioned above.

In our developed synthetic scheme, we firstly prepared 1-μm $Cu_3(BTC)_2$ crystals with Cu_2O microcrystals as a precursor and in the presence of polyvinylpyrrolidone (PVP). As shown in Figure S1 in the Supporting Information, the $Cu_3(BTC)_2$ microcrystals have a well-defined octahedral profile with a very narrow size distribution. The resulting $Cu_3(BTC)_2$ microcrystals exhibit satisfactory capability to be suspended in ethanol solution, which allowed us to employ a hydrolysis method to coat TiO_2 onto the microcrystals. Figure 1b shows a transmission electron microscopy (TEM) image of the sample, which indicates that a layer of shell formed on the microcrystals. According to the statistics (Figure S2, Supporting Information), the average shell thickness is about 210 nm. The scanning electron microscopy (SEM) image in Figure 1c suggests

R. Li,[+] J. Hu,[+] M. Deng, H. Wang, X. Wang, Y. Hu, Prof. H.-L. Jiang, Prof. J. Jiang, Prof. Q. Zhang, Prof. Y. Xie, Prof. Y. Xiong
Hefei National Laboratory for Physical Sciences at the Microscale
Collaborative Innovation Center of Chemistry for Energy Materials (iChEM)
Synergetic Innovation Center of Quantum Information & Quantum Physics
and School of Chemistry and Materials Science
University of Science and Technology of China
Hefei, Anhui 230026, P. R. China
E-mail: jiangj1@ustc.edu.cn; qunzh@ustc.edu.cn; yjxiong@ustc.edu.cn

M. Deng
Guizhou Provincial Key Laboratory of Computational Nano-Material Science
Guizhou Normal College
Guiyang 550018, China

[+]These authors contributed equally to this work

DOI: 10.1002/adma.201400428

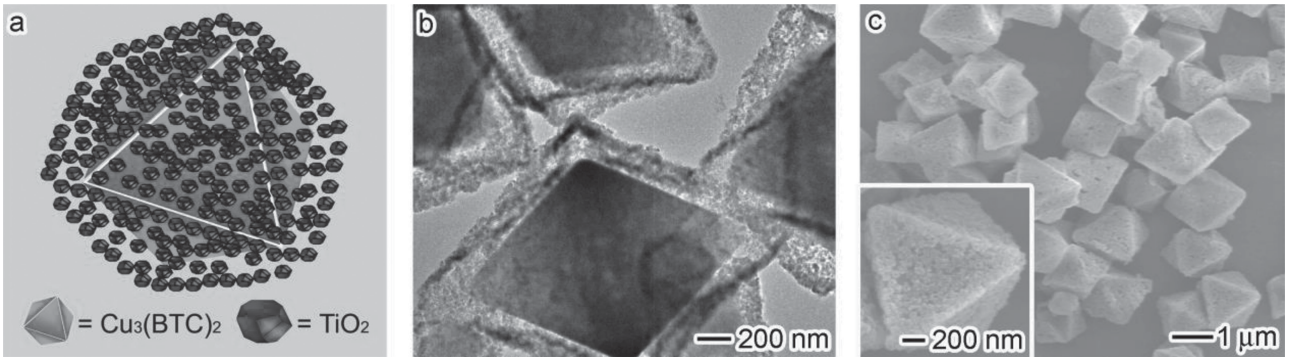

Figure 1. a) Structural illustration, b) TEM, and c) SEM images of the synthesized $Cu_3(BTC)_2$@TiO_2 core-shell structures.

that the core-shell structures inherit the octahedral profile from the $Cu_3(BTC)_2$ cores and have a relatively rough surface. To resolve the core-shell structures better, we employed high-resolution TEM (HRTEM) to characterize the sample. As revealed in Figure S3 in the Supporting Information, each shell is composed of tiny 10–20 nmTiO_2 nanocrystals, which builds a porous surface. The observed lattice fringes can be assigned to the (101) face of anatase TiO_2. The X-ray diffraction (XRD) and energy-dispersive X-ray spectra (EDS) (Figure S4 and S5, Supporting Information) confirm that the sample is a hybrid structure between anatase TiO_2 and $Cu_3(BTC)_2$. As determined by inductively coupled plasma mass spectrometry (ICP-MS), the ratio of TiO_2 to $Cu_3(BTC)_2$ is approximately 0.5. The uniform coating of TiO_2 shells can only be achieved on $Cu_3(BTC)_2$ microcrystals that are prepared with solid Cu precursors and in the presence of PVP (Figure S6, Supporting Information).

The developed core-shell structures retain well the ability of $Cu_3(BTC)_2$ to capture CO_2 despite the presence of TiO_2 shells, as confirmed by CO_2-sorption measurements. **Figure 2**a shows the representative N_2 adsorption–desorption isotherms for the bare $Cu_3(BTC)_2$ and $Cu_3(BTC)_2$@TiO_2 core-shell structures, respectively. The sample of bare $Cu_3(BTC)_2$ attains a total surface area (S_{BET}) of 1183 m^2 g^{-1}, while the S_{BET} value based on the total weight for $Cu_3(BTC)_2$@TiO_2 core-shell structures is

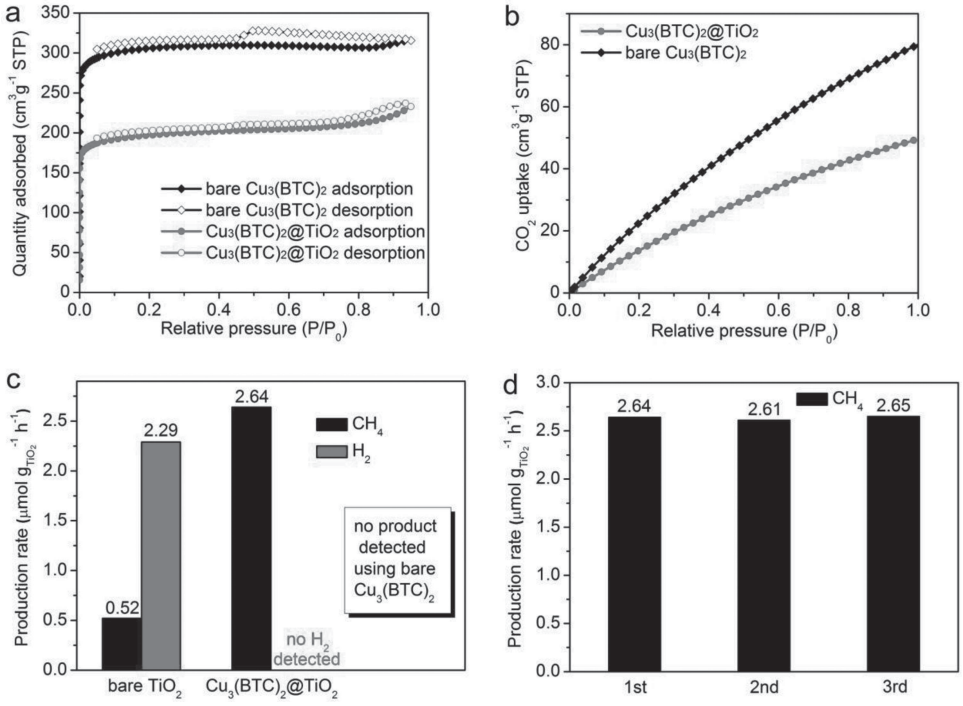

Figure 2. a) N_2 adsorption–desorption isotherms and b) CO_2 adsorption behaviors for $Cu_3(BTC)_2$@TiO_2 core-shell structures and bare $Cu_3(BTC)_2$, respectively. The data are plotted based on the total weights of materials. c) Production yields of CH_4 and H_2 from CO_2 using $Cu_3(BTC)_2$@TiO_2 core-shell structures as photocatalysts under UV irradiation for 4 h, in reference to bare TiO_2 nanocrystals calculated by the weight of photoactive TiO_2. Bare $Cu_3(BTC)_2$ microcrystals were also used as a reference. 100 mg bare TiO_2, 200 mg bare $Cu_3(BTC)_2$, and 300 mg $Cu_3(BTC)_2$@TiO_2 hybrid structures were used in the measurements. The samples were carefully pretreated to remove any carbon contaminants (see Experimental Section). No CO or alcohol products were found for any samples, and formation of O_2 was observed for the oxidation. d) Production yields of CH_4 with $Cu_3(BTC)_2$@TiO_2 photocatalyst in recycling tests.

relatively low (756 m^2 g^{-1}). Nevertheless, the decrease in S_{BET} after TiO_2 coating is reasonable, as the TiO_2 shells account for 1/3 of the total weight and do not have as large a surface area as the MOF structure. More specifically, the curves for $Cu_3(BTC)_2$ sample are a type I isotherm, which suggests that this sample is a microporous material.[17] The $Cu_3(BTC)_2$@TiO_2 core-shell structures show a similar feature at low pressure ($P/P_0 = 0.01$) and a slight hysteresis in the desorption curve, which reveals that the $Cu_3(BTC)_2$ core contributes to microporosity and the TiO_2 shell contains a few meso-/macropores (refer to the pore-size distribution in Figure S7 in the Supporting Information). The CO_2-adsorption behaviors of samples at 298 K are shown in Figure 2b. The bare $Cu_3(BTC)_2$ and $Cu_3(BTC)_2$@TiO_2 core-shell structures exhibit CO_2 uptakes of 80.75 and 49.17 cm^3 g^{-1}, respectively, based on the total weight. Given that TiO_2 is not a material with a distinct effect on CO_2 adsorption, the CO_2 uptake of $Cu_3(BTC)_2$ component in the core-shell structures (roughly 73.75 cm^3 g^{-1}) is comparable to that of bare $Cu_3(BTC)_2$ and superior to that of bare TiO_2 (Figure S8, Supporting Information); this result suggests that CO_2 molecules can easily pass through the macroporous TiO_2 shells and are adsorbed on the microporous $Cu_3(BTC)_2$ cores.

After acquiring the structural characteristics, we further examined the photocatalytic performance of the developed hybrid structures. Figure 2c shows the conversion yields of CO_2 into CH_4 and other products by using our sample as a photocatalyst under UV illumination, in comparison with the bare TiO_2 nanocrystals (see morphologies in Figure S8 in the Supporting Information). This experiment demonstrates superior efficiency in the CO_2 conversion when using our designed core-shell structures to that when using their counterparts: i) the yield of CH_4 is over five times that when using the bare TiO_2; ii) the selectivity of CH_4 to other products (particularly H_2) was significantly improved in our design, which represents the selectivity of CO_2 to H_2O in the photocatalytic reduction. Although both TiO_2 and $Cu_3(BTC)_2$ can absorb UV light (refer to the UV–vis spectra in Figure S9 in the Supporting Information), the bare $Cu_3(BTC)_2$ does not possess photocatalytic activity because its conjugated structure does not favor charge separation. In addition to the advantage in conversion efficiency, the designed structures exhibit excellent performance stability in a recycling test (Figure 2d), with strong resistance to morphology and composition changes (see Figure S10, Supporting Information).

The information above clearly demonstrates the niche of our $Cu_3(BTC)_2$@TiO_2 core-shell structures in photocatalysis. We are now in a position to try to understand the mechanisms behind the function of our structure. Given that the production of CH_4 is an eight-electron process,[2] the high reaction selectivity indicates that higher electron density is achieved in our hybrid structures than in bare TiO_2, which is attributable to the improved electron–hole separation. Our transient photocurrent response measurements (Figure S11, Supporting Information) show that the photocurrent for $Cu_3(BTC)_2$@TiO_2 core-shell structures is significantly higher than that for bare TiO_2, which suggests enhanced efficiency in separating the photogenerated electron–hole pairs. The enhanced charge-separation efficiency was also verified by incident-photon-to-current conversion efficiency (IPCE) characterizations (Figure S12, Supporting Information). Further details relating to the involved dynamical charge behavior were revealed by ultrafast transient absorption (TA) spectroscopy.[24] By using a femtosecond UV pump/white-light-continuum probe scheme (details in Supporting Information), we interrogated the $Cu_3(BTC)_2$@TiO_2 hybrid structures with reference to bare TiO_2 and bare $Cu_3(BTC)_2$.

Given that the bandgap of TiO_2 is around 3.2 eV,[25] a 350 nm (center wavelength; ca. 3.5 eV) pump laser was used. The probing region was set within 400–750 nm (1.6–3.1 eV). The registered TA kinetic profiles are almost independent of the probe wavelengths; we therefore show here a set of representative data taken at 450, 600, and 600 nm (center wavelength) for bare TiO_2, bare $Cu_3(BTC)_2$, and $Cu_3(BTC)_2$@TiO_2, respectively (**Figure 3**a). The relevant mechanisms are schematically illustrated in Figure 3b. For bare TiO_2, the negative-value stimulated emission (SE) signals build up within the instrument response function (ca.100 fs) and then decay with a typical recovery time

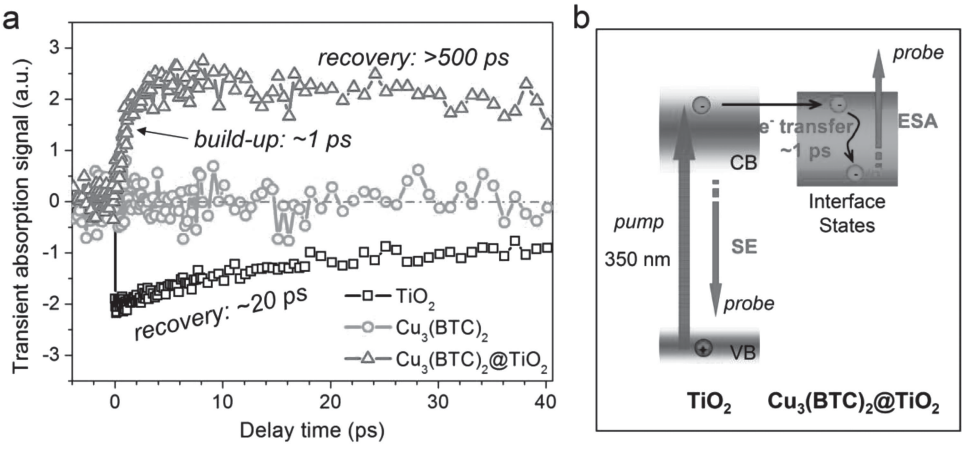

Figure 3. a) Ultrafast transient absorption signal as a function of probe delay for bare TiO_2 (probed at 450 nm), bare $Cu_3(BTC)_2$ (probed at 600 nm), and $Cu_3(BTC)_2$@TiO_2 hybrid structures (probed at 600 nm). All the data were recorded with a 350 nm pump. The time constants given in the plot are derived from the exponential fitting of the relevant kinetic traces. b) Schematic illustration of the involved electron behavior under the femtosecond pump–probe measurements. VB, valence band; CB, conduction band; SE, stimulated emission; ESA, excited-state absorption.

constant of ca. 20 ps. The former process reflects the instantaneous electron transfer from the conduction band (CB) to the surface states that lie below the CB bottom (not depicted in Figure 3b), while the latter process is responsible for the electron–hole recombination that would undesirably consume the photoexcitation energy. Such transient SE signals probed in the region 400–750 nm are consistent with the documented photoluminescence from bare TiO_2.[25] As for bare $Cu_3(BTC)_2$, however, no TA signals are discernable over this particular probing region, albeit it can absorb 350 nm light (refer to Figure S9, Supporting Information). This null-signal observation arises most likely as a result of the absence of electronic states of $Cu_3(BTC)_2$ on resonance with the probing laser in the 400–750 nm region.

We now turn our attention to the distinctly different TA kinetic trace of $Cu_3(BTC)_2@TiO_2$, which features positive-value excited-state absorption (ESA) signals with an initial build-up (ca. 1 ps, typically), followed by a long-time recovery (>500 ps, typically). Based on this observation, it would be safe to infer that the formation of the interface states between TiO_2 and $Cu_3(BTC)_2$ most likely leads to effective shuttering of the electron-transfer channels from the TiO_2 CB to its surface states; if otherwise, the negative-value SE signals associated with the surface states of TiO_2 would by no means be overwhelmed by the positive-value ESA signals. Consequently, the photoexcited electrons in the TiO_2 CB should transfer to (and then relax within) the adjacent interface states of $Cu_3(BTC)_2@TiO_2$, and are subsequently probed by means of ESA to the higher-lying excited states of the $Cu_3(BTC)_2@TiO_2$ hybrid. As such, the observed ca.1 ps build-up time (much longer than the instrument response function of ca. 100 fs) should account for this electron-transfer/relaxation process (see Figure 3b). The absence of the transient SE signals suggests that the designed hybrid system is intrinsically robust in improving the efficiency of electron–hole separation; the subsequent recovery of the ESA signals appears rather slow (>500 ps). This kinetic behavior indicates that the photoexcited electrons localized in the interface states of $Cu_3(BTC)_2@TiO_2$ are sufficiently long-lived, a feature that should be beneficial for the activation of CO_2 adsorbed on the $Cu_3(BTC)_2$.

From the analysis above, it can be concluded that in the hybrid structures the TiO_2 is photoexcited to generate electron–hole pairs and the electrons are transferred to the $Cu_3(BTC)_2$. CO_2 can be adsorbed on the Cu sites during CO_2 uptake by the $Cu_3(BTC)_2$ MOFs.[18–20] Thus it is safe to propose that during the photocatalysis the CO_2 reduction takes place on the Cu sites of $Cu_3(BTC)_2$ while the oxidation occurs on the TiO_2. The improved selectivity of CO_2 to H_2O in the photocatalytic reduction (i.e., the production selectivity of CH_4 to H_2) is the key to our work. As demonstrated,[2] this selectivity is related to two major factors: i) the activation sites for the reduction reactions; ii) the charge-separation efficiency, given that the production of CH_4 is an eight-electron process. The improved efficiency of charge separation in our designed hybrid system was proven by ultrafast spectroscopy. In terms of the activation sites, the Cu sites have much higher selectivity for the reduction of CO_2 than does the TiO_2 surface (i.e., the case of bare TiO_2).[2,4,26,27] To evaluate the situation in our $Cu_3(BTC)_2$ system, theoretical simulations were performed to examine whether the CO_2 molecules can be activated well on the Cu sites of the MOFs upon receiving the photoexcited electrons from the TiO_2. As the whole reaction pathway of CO_2 towards CH_4 product has been extensively investigated,[2] our simulations mainly focused on the molecular activation of CO_2 facilitated by the charged MOFs.

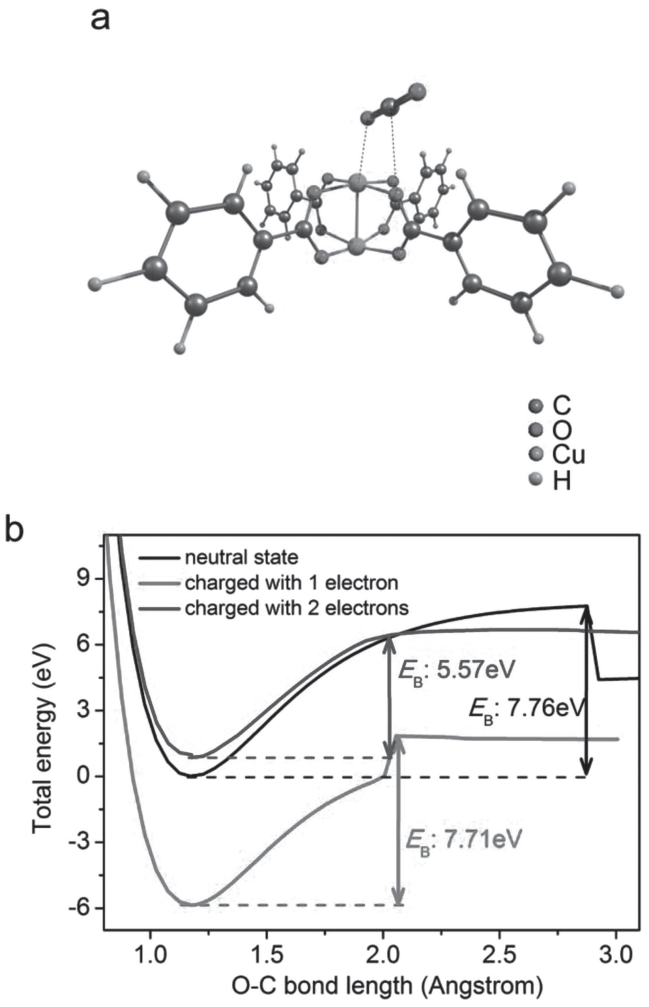

Figure 4. a) The optimized structure for CO_2 adsorbed on $Cu_3(BTC)_2$. b) Potential energy surfaces along the O–C bond length for the activation of the CO_2 molecule adsorbed on $Cu_3(BTC)_2$ in the neutral state or the states charged with one or two electrons, from which the CO_2 activation energies (E_B) were deducted. The data were extracted from first-principles simulations (details in Supporting Information).

The activation of CO_2 molecules is normally triggered by two-electron charges.[28] From first-principles simulations (**Figure 4**a), we reveal that addition of one- or two-electron charges can greatly improve the adsorption of CO_2 to $Cu_3(BTC)_2$, with the calculated adsorption energy increasing from 0.36 to 0.54 or 1.05 eV, respectively. The simulated potential energy surfaces along the variation of the O–C bond of the CO_2 molecule adsorbed on $Cu_3(BTC)_2$ are plotted in Figure 4b. The addition of a one-electron charge can barely alter the activation-energy barrier (E_B) for CO_2, while the two-electron charge injection substantially lowers the E_B from 7.76 to 5.57 eV. Thus, upon receiving the photoexcited electrons from TiO_2,

$Cu_3(BTC)_2$ can turn into an active catalytic material for the activation of CO_2 molecules. The MOF unit used for the CO_2 activation simulations was verified to fully represent the behavior of the entire MOF network, as indicated by the density of state (DOS) data in Figure S13 in the Supporting Information.

In conclusion, we proposed a MOF@semiconductor core-shell structure with a macroporous shell to generate excitons and a microporous core to capture gas molecules. As demonstrated by ultrafast spectroscopy, the photogenerated electrons can be effectively transferred from the semiconductor to the MOF, which not only facilitates charge separation in the semiconductor but supplies energetic electrons to gas molecules adsorbed on the MOF. We show that CO_2 can easily penetrate the shells and become captured in the cores, followed by photocatalytic reduction to CH_4 with dramatically improved performance in terms of both activity and selectivity. It is anticipated that the present work will open a door to implementing MOF structures in photocatalyst design for gaseous reactions, as well as enable deeper understanding of charge transfer in novel hybrid materials.

Experimental Section

Synthesis of $Cu_3(BTC)_2$ @TiO_2 Core-Shell Structures: $Cu_3(BTC)_2$ microcrystals (5 mg) were dispersed in 10 mL ethanol, and then mixed with 50 μL of tetrabutyl titanate. The dispersion was stirred at room temperature for 15 min, and then mixed with 700 μL of water and 21 μL of HF. (*Caution*: HF is extremely corrosive and a contact poison, and it should be handled with extreme care! HF solution should be stored in Teflon containers while in use.) Subsequently, the dispersion was stirred at room temperature for another 15 min, then moved to a 20-mL Teflon autoclave liner and heated at 180 °C for 12 h. The resulting particles were isolated by centrifugation and washed with ethanol three times. Finally, the obtained powder was dried at 60 °C in vacuum.

Photocatalytic Conversion of CO_2: The measurements were performed with a home-made stainless-steel photocatalytic reactor. The set-up of the photocatalytic system is illustrated in Figure S14 in the Supporting Information. In the reactor, the quartz tube had a length of 340 mm and an outer diameter of 20 mm. The total volume of the reactor was about 100 mL. Solid catalysts were mounted on a glass sinter which was placed in a quartz boat containing 5 mL water. In the measurements, 100 mg bare TiO_2, 200 mg bare $Cu_3(BTC)_2$, and 300 mg $Cu_3(BTC)_2$@TiO_2 hybrid structures were used, respectively, to keep the photoactive materials and CO_2-adsorptive materials at the same weights. Then the quartz boat was placed into the quartz tube. In this configuration, the catalysts were not immersed into the liquid water but surrounded by H_2O vapor and CO_2. Prior to the test, the catalysts were carefully pretreated to remove any possible organic contaminants: i) The samples were baked in a vacuum oven at 150 °C for 24 h to remove residues of alcohol solvents and other organic agents; ii) they were loaded in the reactor and UV irradiated then exposed to H_2O vapor in 0.15 MPa Ar, which can effectively eliminate trace carbon residues from our samples and reactor.[29] Further, the pretreated samples were tested in 0.15 MPa fresh Ar in the absence of CO_2 but in the presence of H_2O; this showed no production of CH_4 and thus confirmed that our following measurements were free of any carbon contaminants. Then the reactor loaded with the catalysts was purged with CO_2 at 50 mL min^{-1} for 20 min. Subsequently, the valves were closed, and the pressure of CO_2 was regulated to 0.15 MPa. The temperature of the reactor was kept at 313 K. A 300 W xenon arc lamp (SolarEdge700) was used as the light source for the photocatalytic reaction, with a 400 nm short-wave-pass cut-off filter (i.e., λ < 400 nm). The photocatalytic reaction was performed for 4 h. The amounts of CH_4 and H_2 evolved were determined using the flame ionization detector (FID) and thermal conductivity detector (TCD) of a gas chromatograph (GC, 7890A, Ar carrier, Agilent). CO was converted to CH_4 by a methanation reactor and then analyzed by using the FID detector of the GC; no signals for CO were observed. No signals for alcohols were observed in this way, either. The CO_2 source was also analyzed by using the GC FID, and the resulting signals were used as a blank that was deducted from our photocatalytic data, to avoid any influence of impurities in the CO_2 source. The formation of O_2 was also observed for oxidation. Three replicates were collected for each catalyst with relative error < 10 %.

Ultrafast Spectroscopic Characterizations: The ultrafast transient absorption data were recorded on a modified pump–probe spectrometer (ExciPro, CDP) in combination with an amplified femtosecond laser system (Coherent). The schematic of the optical layout is shown in Figure S15 in the Supporting Information. The experimental details are in the Supporting Information. The samples were dispersed in ethanol for all pump–probe characterizations, which were performed under ambient conditions.

Supporting Information

Supporting Information is available from the Wiley Online Library or from the author.

Acknowledgements

This work was financially supported by the 973 Program (No. 2014CB848900, 2010CB923300), the NSFC (No. 21101145, 11321503, 91127042, 21173205, 91221104), the Recruitment Program of Global Experts, the CAS Hundred Talent Program, the CAS Strategic Priority Research Program B (No. XDB01020000), the Fundamental Research Funds for the Central Universities (No. WK2060190025), and the Construction Project for Guizhou Provincial Key Laboratories (ZJ[2011]4007). The authors are grateful to Prof. Yi Luo for helpful discussions.

Received: January 27, 2014
Revised: March 26, 2014
Published online: May 23, 2014

[1] A. L. Linsebigler, G. Lu, J. T. Yates, Jr., *Chem. Rev.* **1995**, *95*, 735.
[2] S. C. Roy, O. K. Varghese, M. Paulose, C. A. Grimes, *ACS Nano* **2010**, *4*, 1259.
[3] S. N. Habisreutinger, L. Schmidt-Mende, J. K. Stolarczyk, *Angew. Chem. Int. Ed.* **2013**, *52*, 7372.
[4] Q. Zhai, S. Xie, W. Fan, Q. Zhang, Y. Wang, W. Deng, Y. Wang, *Angew. Chem. Int. Ed.* **2013**, *52*, 5776.
[5] K. Sumida, D. L. Rogow, J. A. Mason, T. M. McDonald, E. D. Bloch, Z. R. Herm, T.-H. Bae, J. R. Long, *Chem. Rev.* **2012**, *112*, 724.
[6] R. Banerjee, A. Phan, B. Wang, C. Knobler, H. Furukawa, M. O'Keeffe, O. M. Yaghi, *Science* **2008**, *319*, 939.
[7] J. Liu, P. K. Thallapally, B. P. McGrail, D. R. Brown, J. Liu, *Chem. Soc. Rev.* **2012**, *41*, 2308.
[8] A. Ö. Yazaydin, R. Q. Snurr, T. H. Park, K. Koh, J. Liu, M. D. LeVan, A. I. Benin, P. Jakubczak, M. Lanuza, D. B. Galloway, J. J. Low, R. R. Willis, *J. Am. Chem. Soc.* **2009**, *131*, 18198.
[9] M. P. Suh, H. J. Park, T. K. Prasad, D.-W. Lim, *Chem. Rev.* **2012**, *112*, 782.
[10] B. Chen, S. Xiang, G. Qian, *Acc. Chem. Res.* **2010**, *43*, 1115.
[11] L. E. Kreno, K. Leong, O. K. Farha, M. Allendorf, R. P. Van Duyne, J. T. Hupp, *Chem. Rev.* **2012**, *112*, 1105.

[12] J.-R. Li, J. Sculley, H.-C. Zhou, *Chem. Rev.* **2012**, *112*, 869.
[13] J. S. Seo, D. Whang, H. Lee, S. I. Jun, J. Oh, Y. J. Jeon, K. Kim, *Nature* **2000**, *404*, 982.
[14] L. Ma, C. Abney, W. Lin, *Chem. Soc. Rev.* **2009**, *38*, 1248.
[15] A. Corma, H. García, F. X. Llabrés i Xamena, *Chem. Rev.* **2010**, *110*, 4606.
[16] P. Horcajada, R. Gref, T. Baati, P. K. Allan, G. Maurin, P. Couvreur, G. Férey, R. E. Morris, C. Serre, *Chem. Rev.* **2012**, *112*, 1232.
[17] S. S. Y. Chui, S. M. F. Lo, J. P. H. Charmant, A. G. Orpen, I. D. Williams, *Science* **1999**, *283*, 1148.
[18] C. Montoro, E. García, S. Calero, M. A. Pérez-Fernández, A. L. López, E. Barea, J. A. R. Navarro, *J. Mater. Chem.* **2012**, *22*, 10155.
[19] J. Yu, Y. Ma, P. B. Balbuena, *Langmuir* **2012**, *28*, 8064.
[20] S. Ye, X. Jiang, L.-W. Ruan, B. Liu, Y.-M. Wang, J.-F. Zhu, L.-G. Qiu, *Microporous Mesoporous Mater.* **2013**, *179*, 191.
[21] C. H. Kuo, Y. Tang, L. Y. Chou, B. T. Sneed, C. N. Brodsky, Z. Zhao, C. K. Tsung, *J. Am. Chem. Soc.* **2012**, *134*, 14345.
[22] W. W. Zhan, Q. Kuang, J. Z. Zhou, X. J. Kong, Z. X. Xie, L. S. Zheng, *J. Am. Chem. Soc.* **2013**, *135*, 1926.
[23] K. E. deKrafft, C. Wang, W. Lin, *Adv. Mater.* **2012**, *24*, 2014.
[24] P. Hannaford, *Femtosecond Laser Spectroscopy*, Springer, New York, **2005**.
[25] J. W. Liu, J. Li, A. Sedhain, J. Y. Lin, H. X. Jiang, *J. Phys. Chem. C* **2008**, *112*, 17127.
[26] O. K. Varghese, M. Paulose, T. J. LaTempa, C. A. Grimes, *Nano Lett.* **2009**, *9*, 731.
[27] Y. Hori, I. Takahashi, O. Koga, N. Hoshi, *J. Phys. Chem. B* **2002**, *106*, 15.
[28] T. Inoue, A. Fujishima, S. Konishi, K. Honda, *Nature* **1979**, *277*, 637.
[29] C. C. Yang, Y. H. Yu, B. van der Linden, J. C. S. Wu, G. Mul, *J. Am. Chem. Soc.* **2010**, *132*, 8398.